Electronic Supplementary Information (ESI)

Photodeposition of a conformal metal oxide nanocoating

Sheng Chu,[a] Roksana Tonny Rashid,[a] Xuedong Liu[b] and Zetian Mi*[a,c]

[a]*Department of Electrical and Computer Engineering, McGill University, 3480 University Street, Montreal, Quebec H3A 0E9, Canada*

[b]*Facility for Electron Microscopy Research, McGill University, 3640 University Street, Montreal, Quebec H3A 0C7, Canada*

[c]*Department of Electrical Engineering and Computer Science, Center for Photonics and Multiscale Nanomaterials, University of Michigan, Ann Arbor, 1301 Beal Avenue, Ann Arbor, MI 48105, USA*

[*]*Corresponding author E-mail: ztmi@umich.edu; Phone: 1 734 764 3963*

Experimental Section

Sample synthesis: Cr_2O_3, Al_2O_3, ZnO, and In_2O_3 nanocoatings were photodeposited on GaN nanowires from an aqueous methanol solution containing the corresponding metal nitrate precursors in a Pyrex chamber with a quartz window. $Cr(NO_3)_3 \cdot 9H_2O$ (99.99%, Sigma Aldrich), $Al(NO_3)_3 \cdot 9H_2O$ (98%, Sigma Aldrich), $Zn(NO_3)_2 \cdot 6H_2O$ (98%, Sigma Aldrich) and $In(NO_3)_3 \cdot 5H_2O$ (99.999%, Strem Chemicals) were used as the precursors. Typically, the preparation conditions were as follows. First, GaN nanowires on Si wafer (~3 cm^{-2}) was put in a Teflon holder and placed in the bottom of glass chamber. Next, 60 mL deionized water (purged with Ar for 10 min prior to the usage), 15 mL methanol, and 20 μL of 0.2 M metal nitrate (i.e., a concentration of 53.3 mM in the mixture solution) were added in the chamber. The chamber was then evacuated for 10 min and irradiated for 30 min using 300 W Xe lamp (2.6 W cm^{-2}, Excelitas Technologies) for the photodeposition of metal oxide nanocoating. GaN nanowires were grown on a 2-inch p-n junction Si wafer by plasma-assisted molecular beam epitaxy (MBE) under nitrogen-rich conditions as described previously.[1] Prior to loading into the MBE chamber, Si wafer was cleaned with acetone, methanol and 10% buffered hydrofluoric acid to remove any organic contaminants and native oxides.

The synthesis procedure for Pt/Cr_2O_3/GaN/n^+–p Si sample was as follows: Cr_2O_3 nanolayer and Pt nanoparticles were photodeposited on GaN nanowires from an aqueous methanol solution in sequential order. The photodeposition process is similar to that described above, except for the use of 5 μL of 0.2 M $Cr(NO_3)_3$ and 15 μL of 0.2 M H_2PtCl_6 (99.9%, Sigma Aldrich) as precursors for the deposition of Cr_2O_3 and Pt, respectively.

The synthesis procedure for Cr_2O_3-coated TiO_2 sample was similar to that of Cr_2O_3-coated GaN, except for the use of TiO_2 on FTO (fluorine doped tin oxide) glass as the substrate and irradiated for 1 h. The TiO_2 on FTO was prepared by a drop casting method. 0.1 g TiO_2 particles (rutile, 99.9%, Sigma Aldrich) were dispersed ultrasonically in 50 mL ethanol, followed by dropping the suspension on FTO substrate and left the solvent evaporated overnight.

Characterization: Scanning electron microscopy (SEM) images were taken on an Inspect F-50 FE-SEM system at an accelerating voltage of 5 keV. Transmission electron microscopy

(TEM) images were acquired on FEI Tecnai G2 F20 microscope operated at 200 keV, with energy-dispersive X-ray spectroscopy (EDX) attached. The nanowires were scratched off from the Si substrate onto a copper grid prior to TEM measurements. X-ray diffraction (XRD) patterns were acquired on a Bruker D8 Discovery X-ray diffractometer with Cu Kα radiation. X-ray photoelectron spectroscopy (XPS) measurements were performed in a Thermo Scientific K-Alpha XPS system with a monochromatic Al Kα source (hν = 1486.6 eV). The binding energies were calibrated using adventitious C1s peak at 284.8 eV. Inductively coupled plasma−atomic emission spectroscopy (ICP-AES) analyses were conducted on a Thermo Scientific iCAP 6000 Series inductively coupled plasma–atomic emission spectroscopy instrument. The samples were digested in 5 ml aqua regia (HNO_3:HCl=1:3) at 95 °C for 3 h. Then the solution was diluted with an additional 5 mL demineralized water prior to the analysis. The NO_2^- content produced during the photodeposition was determined by a Varian Cary 50 UV–Vis spectrometer using a common Griess method.[2] Griess solution was prepared by dissolving 1 g Griess Reagent (G4410, Sigma-Aldrich) into 25 ml of ultrapure water. A calibration curve was obtained from commercial $NaNO_2$ of analytical standards (99.999%, Sigma Aldrich).

Photoelectrochemical (PEC) measurements: PEC experiments were conducted in 0.5 M H_2SO_4 solution with a three-electrode configuration and recorded using a potentiostat (Gamry Instruments, Interface 1000). GaN nanowires on p-n junction Si, Ag/AgCl and Pt wire were employed as the working electrode, reference electrode and counter electrode, respectively. A solar simulator (Newport Oriel) with an AM 1.5G filter was used as the light source, and the illumination intensity at the position of sample was calibrated to be 100 mW cm^{-2}. The scan rate of current-potential (*J-V*) curves was 20 mV/s. The recorded potentials versus Ag/AgCl were converted to versus RHE according to the following equation: E(versus RHE) = E(versus Ag/AgCl) + (0.0591× pH) + 0.1976, where 0.1976 is a conversion factor from the Ag/AgCl electrode to RHE at 25 °C. H_2 product from water splitting was detected by a gas chromatograph (GC, Shimadzu GC-8A) equipped with a thermal conducting detector (TCD), using high purity Ar as carrier gas.

The applied bias photon-to-current efficiency (ABPE) was calculated from *J-V* curve using the following equation:

$$\mathrm{ABPE}(\%)=\left[\frac{J(\mathrm{mA\ cm^{-2}})\times(V_{RHE}-E^{0})(V)}{P_{in}(\mathrm{mW\ cm^{-2}})}\right]\times\ 100\%$$

where J is the photocurrent density; V_{RHE} is the applied potential vs. RHE; E^0 is the equilibrium water reduction potential in 0.5 M H_2SO_4 electrolyte, which is 0 V vs. RHE; P_{in} is the incident illumination power density (AM 1.5G, 100 mW cm^{-2}).

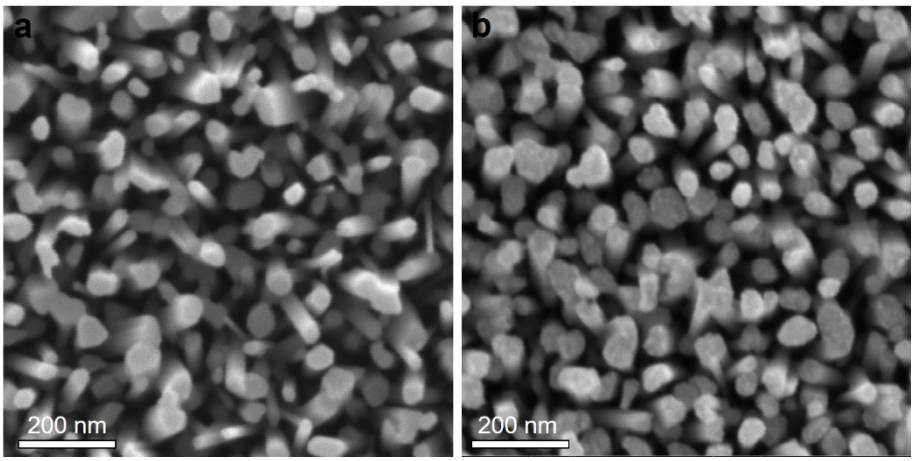

Fig. S1. Top-view SEM images of (a) pristine GaN and (b) Cr_2O_3-deposited GaN.

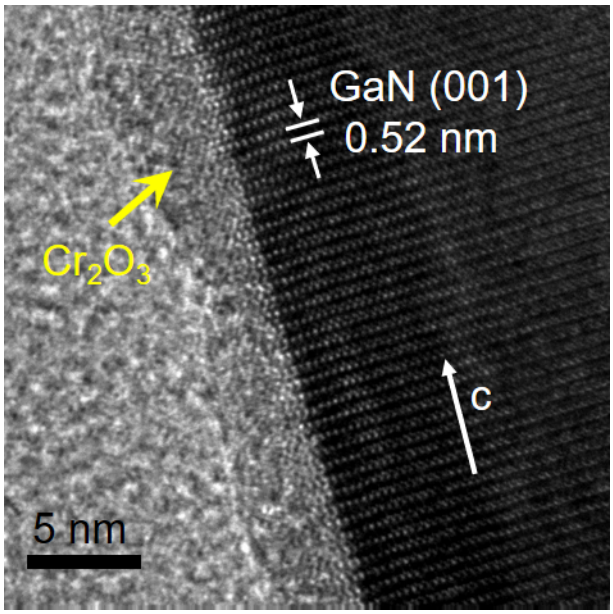

Fig. S2. HRTEM image of Cr_2O_3-deposited GaN sample. It shows Cr_2O_3 coating layer is amorphous and GaN nanowire is single crystalline with the growth direction along the c-axis.

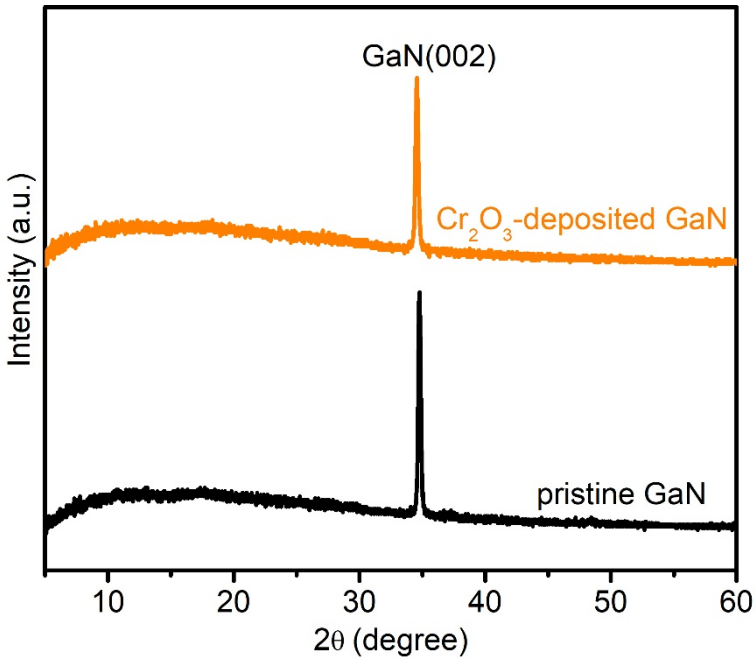

Fig. S3. XRD patterns of pristine GaN and Cr_2O_3-deposited GaN. The two samples display similar patterns attributed to GaN (002) peak. The (002) peak indicates the nanowire growth along the c-axis <0001> direction.

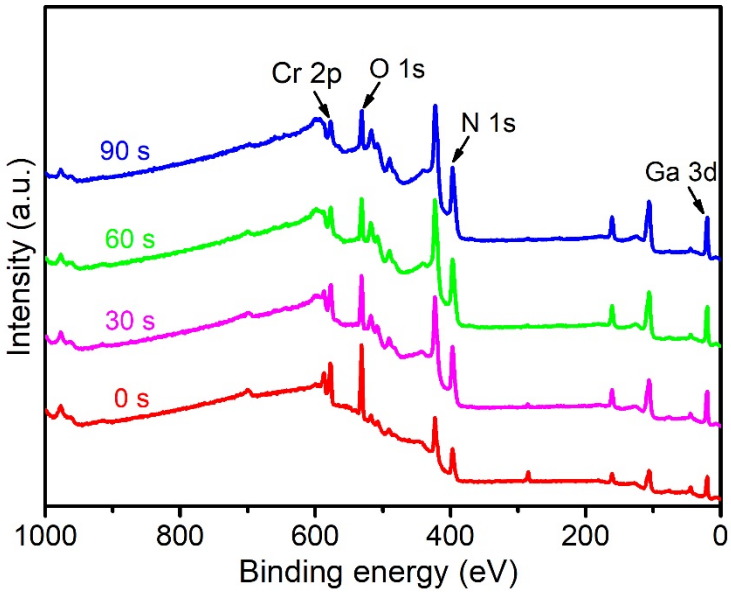

Fig. S4. XPS depth profile of survey spectrum in Cr_2O_3-deposited GaN sample as a function of etching time. As the etching time increased, the O 1s signal decreased progressively, and the N 1s signal increased progressively.

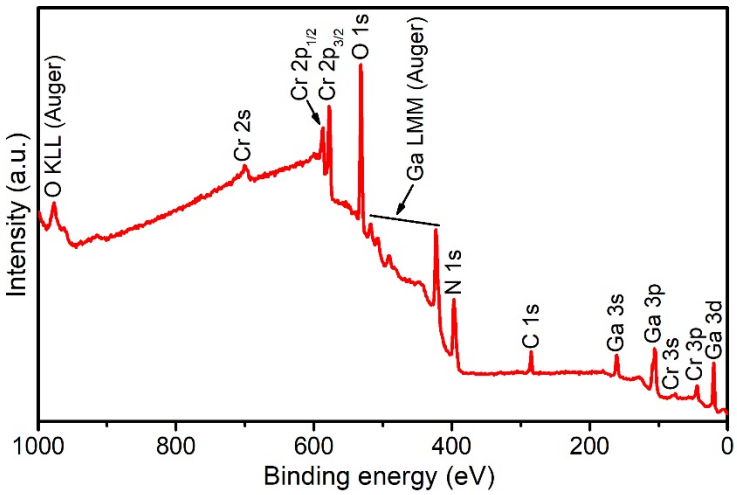

Fig. S5. Survey XPS spectrum of Cr_2O_3-deposited GaN sample. All the spectral features, except the common adventitious C 1s signal, are attributed to constituent element core-levels or Auger lines of Cr_2O_3-deposited GaN.

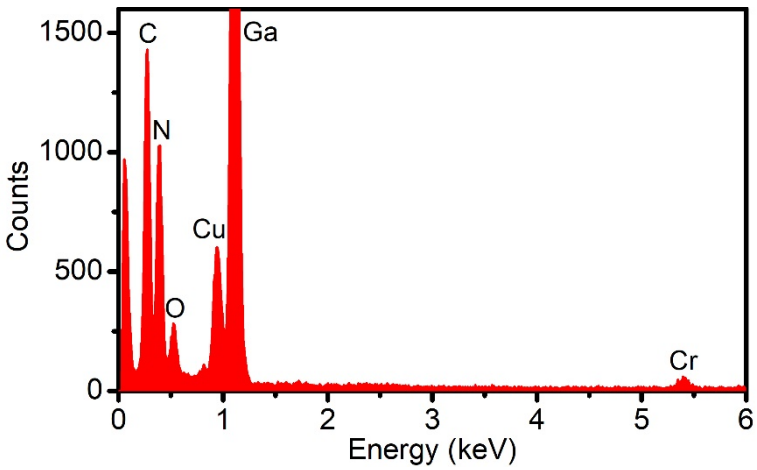

Fig. S6. EDX spectrum of Cr_2O_3-deposited GaN sample. The Cu signal arises from the TEM sample grid.

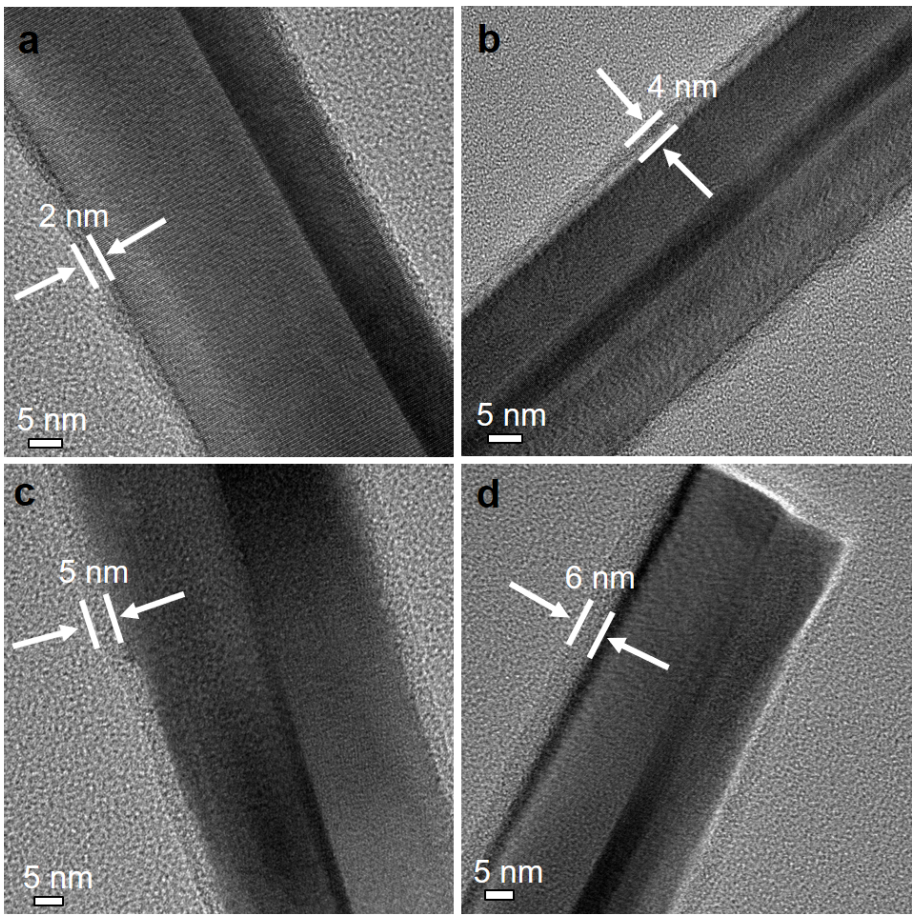

Fig. S7. TEM images of Cr_2O_3-deposited GaN samples with different coating thicknesses by varying the light illumination time of preparation: (a) 10 min, (b) 20 min, (c) 30 min and (d) 40 min. The $Cr(NO_3)_3$ precursor concentration was kept at 53.3 mM for the preparation of all the samples.

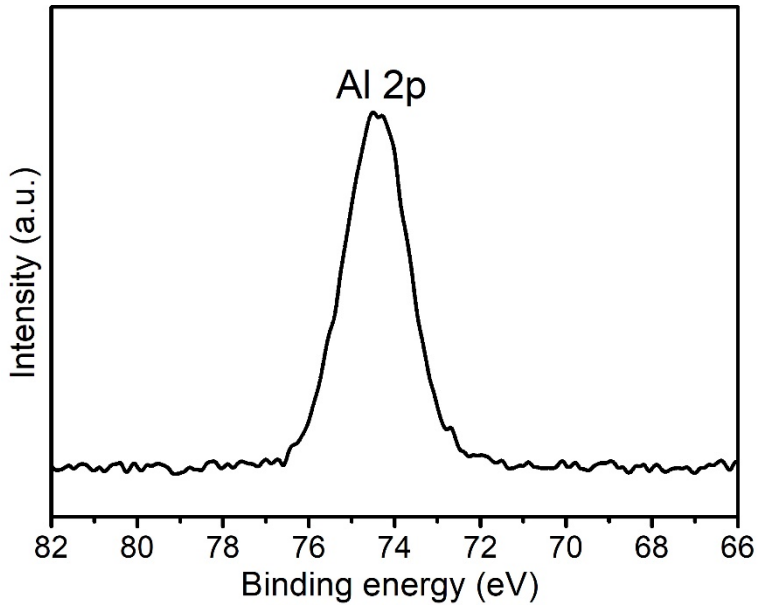

Fig. S8. XPS of Al 2p of Al_2O_3-deposited GaN sample. The Al 2p binding energy at 74.4 eV is assigned to Al^{III} state from Al_2O_3.[3]

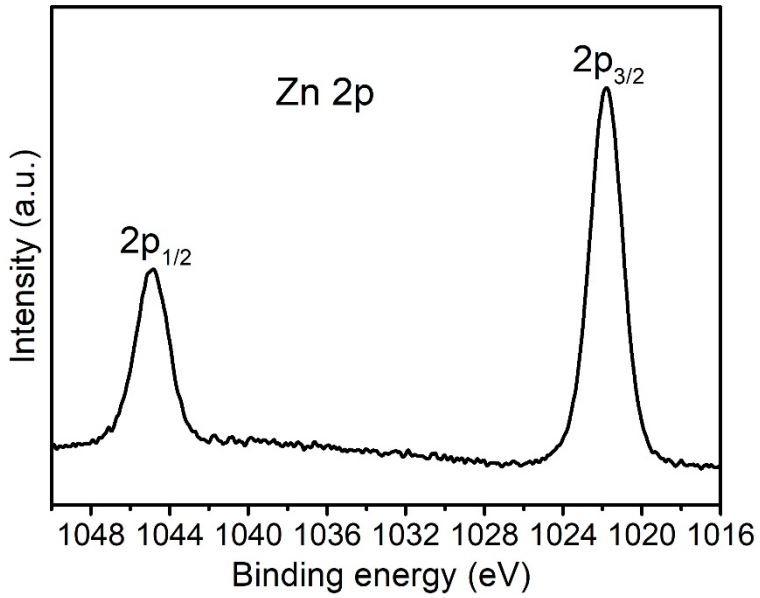

Fig. S9. XPS of Zn 2p of ZnO-deposited GaN sample. The Zn $2p_{3/2}$ binding energy at 1021.8 eV and Zn $2p_{1/2}$ binding energy at 1044.9 eV are assigned to Zn^{II} state from ZnO.[4]

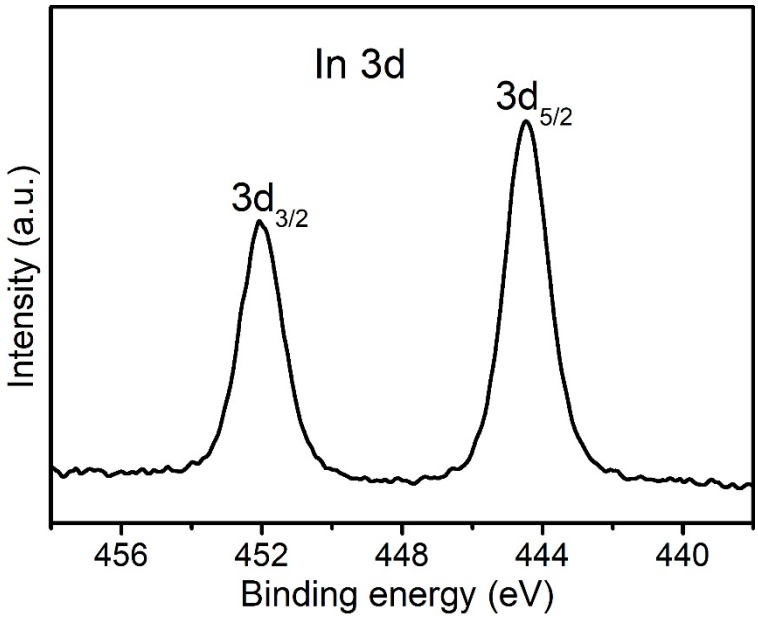

Fig. S10. XPS of In 3d of In_2O_3-deposited GaN sample. The In $3d_{5/2}$ binding energy at 444.5 eV and In $3d_{3/2}$ binding energy at 452.0 eV are assigned to In^{III} state from In_2O_3.[5]

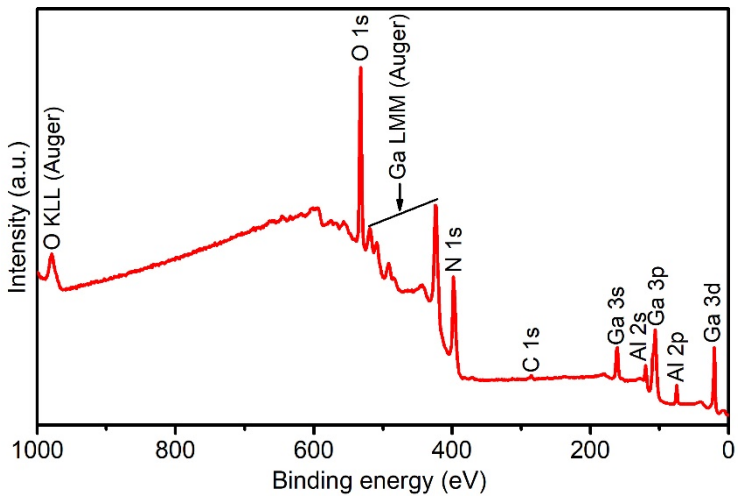

Fig. S11. Survey XPS spectrum of Al_2O_3-deposited GaN sample. All the spectral features, except the common adventitious C 1s signal, are attributed to constituent element core-levels or Auger lines of Al_2O_3-deposited GaN.

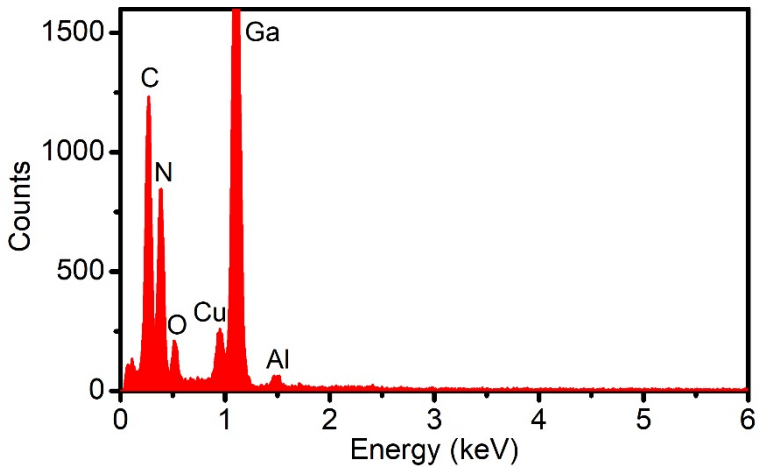

Fig. S12. EDX spectrum of Al_2O_3-deposited GaN sample. The Cu signal arises from the TEM sample grid.

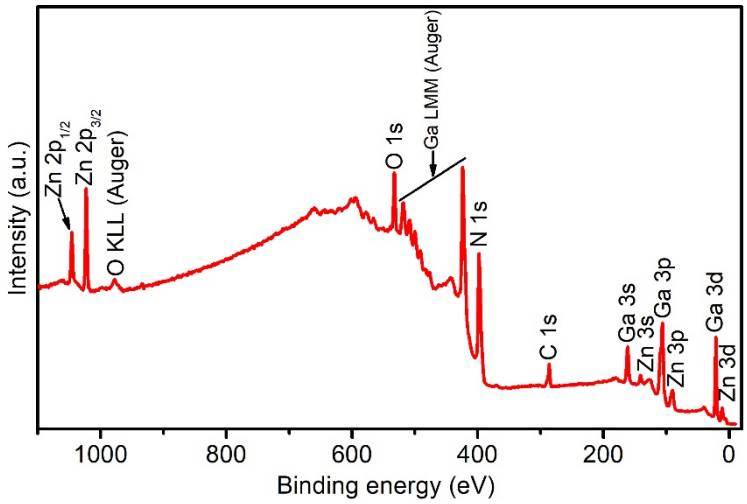

Fig. S13. Survey XPS spectrum of ZnO-deposited GaN sample. All the spectral features, except the common adventitious C 1s signal, are attributed to constituent element core-levels or Auger lines of ZnO-deposited GaN.

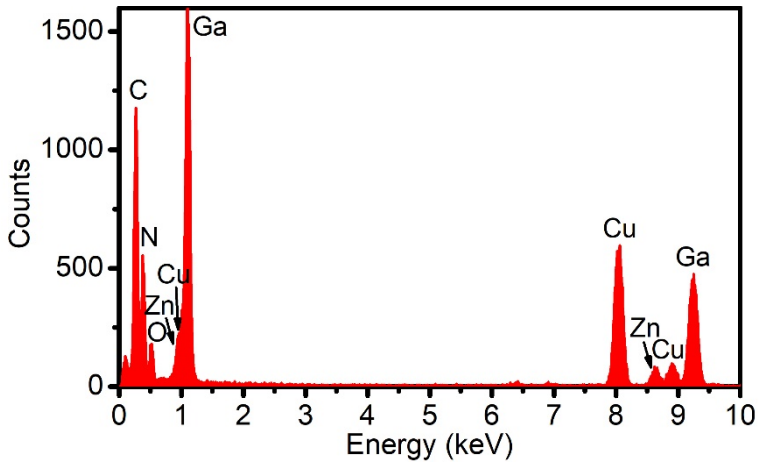

Fig. S14. EDX spectrum of ZnO-deposited GaN sample. The Cu signal arises from the TEM sample grid.

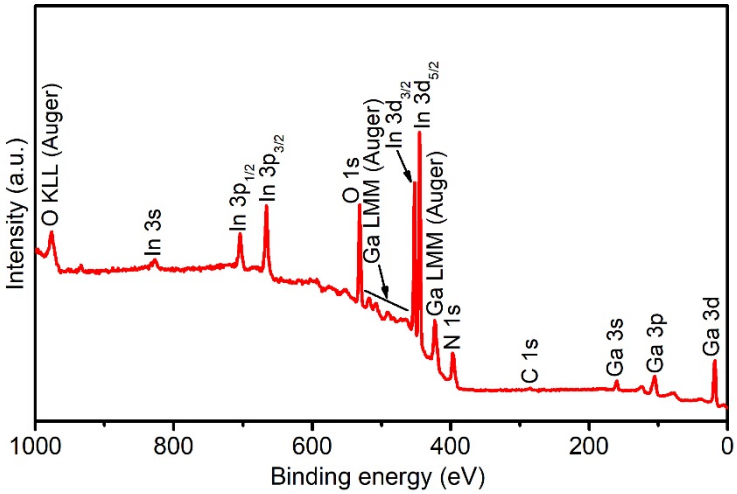

Fig. S15. Survey XPS spectrum of In_2O_3-deposited GaN sample. All the spectral features, except the common adventitious C 1s signal, are attributed to constituent element core-levels or Auger lines of In_2O_3-deposited GaN.

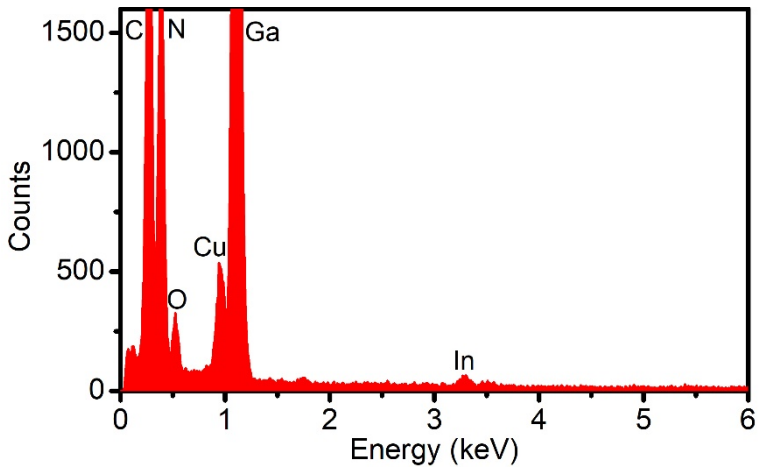

Fig. S16. EDX spectrum of In_2O_3-deposited GaN sample. The Cu signal arises from the TEM sample grid.

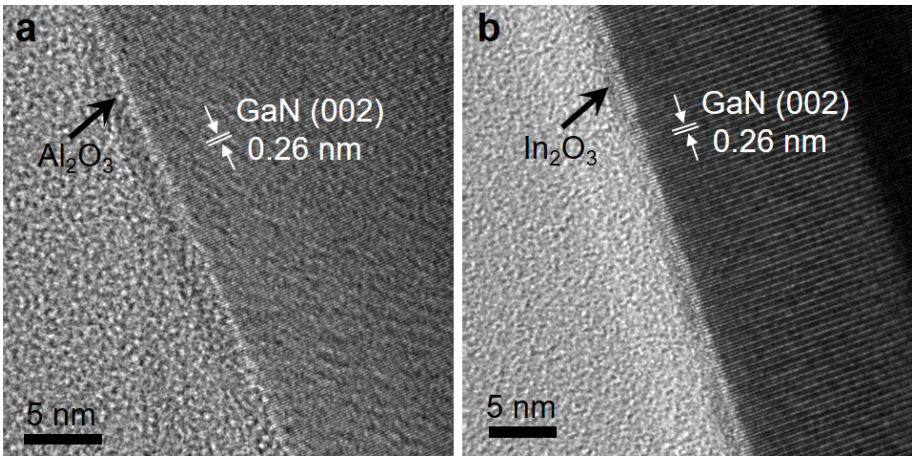

Fig. S17. HRTEM images of (a) Al_2O_3 and (b) In_2O_3-deposited GaN samples, showing both Al_2O_3 and In_2O_3 coating layers are amorphous.

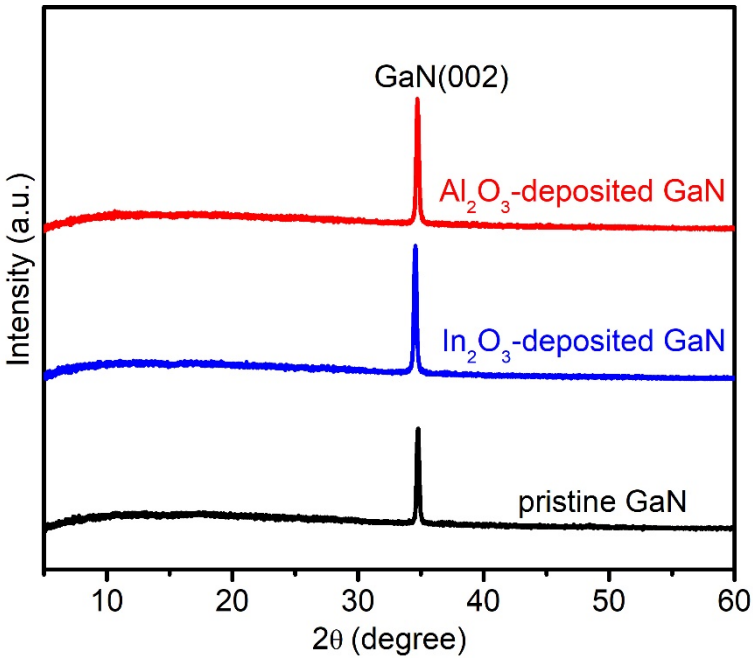

Fig. S18. XRD patterns of pristine GaN, Al_2O_3-deposited GaN and In_2O_3-deposited GaN. All samples display similar patterns attributed to GaN (002) peak.

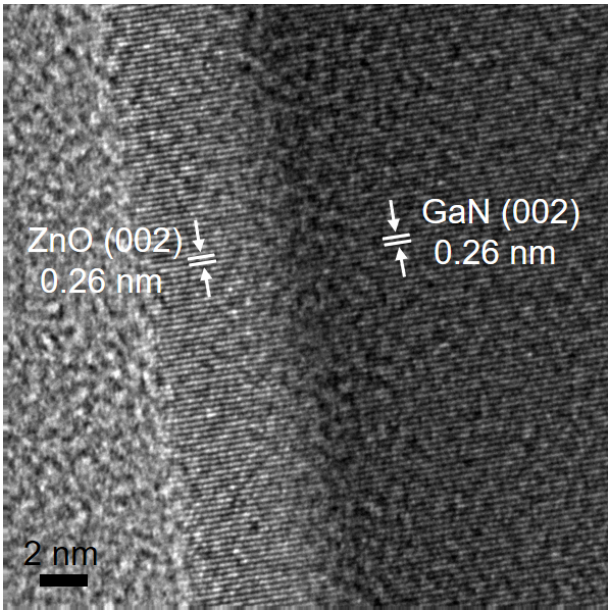

Fig. S19. HRTEM image of ZnO-deposited GaN sample. It shows the crystallinity of ZnO coating layer.

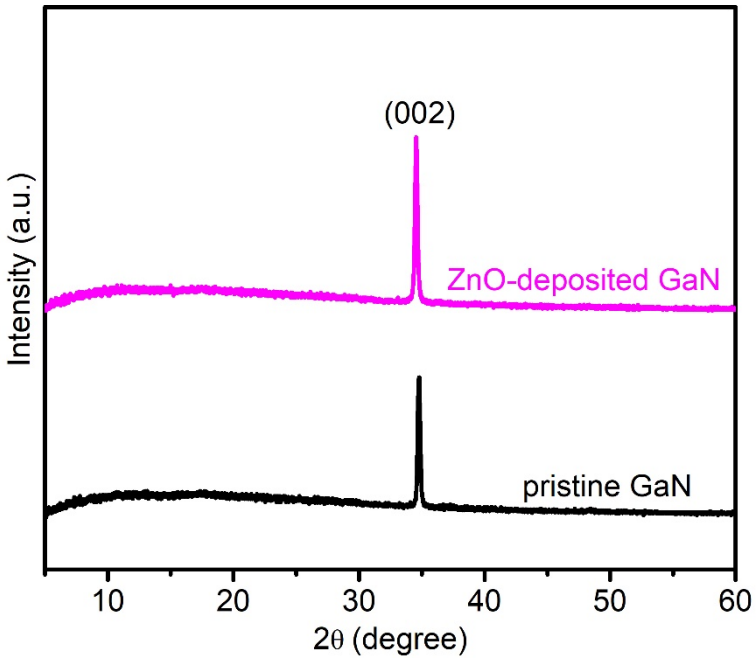

Fig. S20. XRD patterns of pristine GaN and ZnO-deposited GaN. Despite the crystalline structure of ZnO, the (002) peak from ZnO overlaps that of GaN, because the lattice mismatch between the wurtzite ZnO (a = 3.249 Å and c = 5.207 Å) and wurtzite GaN (a = 3.190 Å and c = 5.189 Å) is as small as 0.4% in c-axis lengths.[6] However, we cannot exclude the possibility that no noticeable detection of XRD peaks of crystalline ZnO may be due to its low amounts.

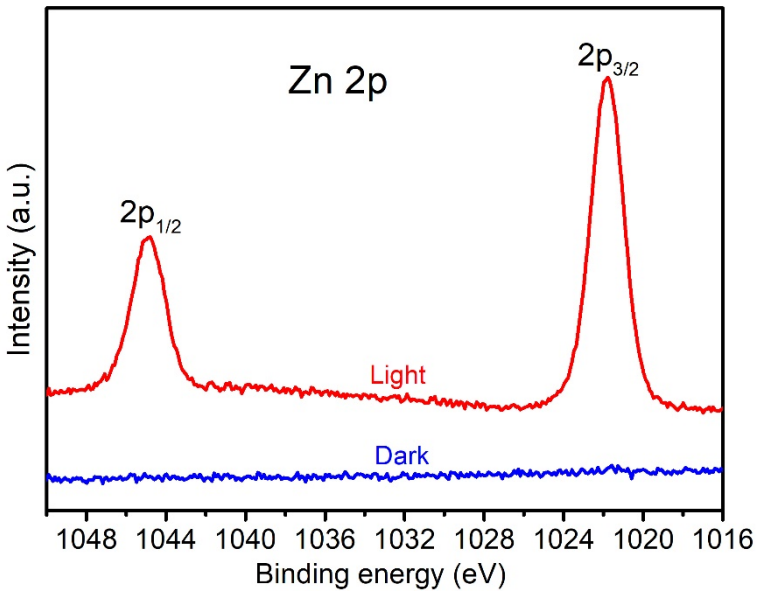

Fig. S21. XPS of Zn 2p of ZnO-deposited GaN samples prepared under dark and light irradiation.

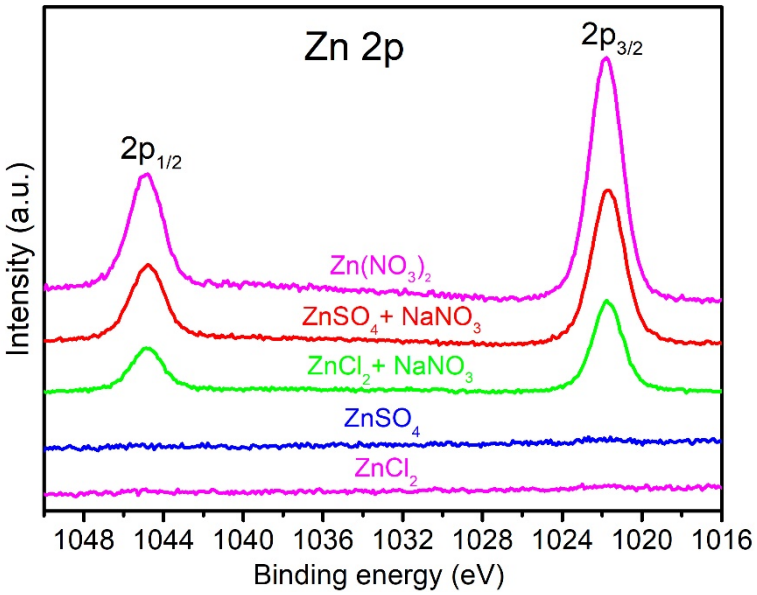

Fig. S22. XPS of Zn 2p of ZnO-deposited GaN samples using different precursors. The added precursor concentration of zinc salts and $NaNO_3$ were 53.3 μM and 106.6 μM, respectively.

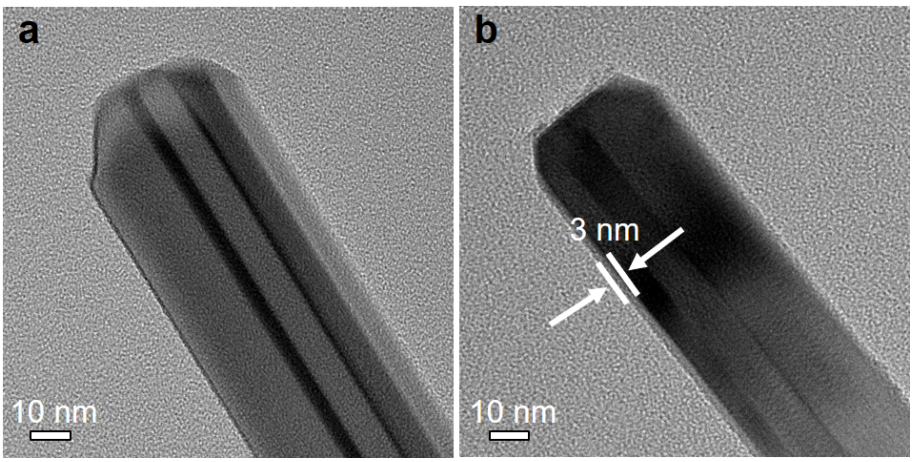

Fig. S23. HRTEM images of ZnO-deposited GaN samples using different precursors. (a) $ZnSO_4$, (b) $ZnSO_4$ + $NaNO_3$. It was found that there was no formation of ZnO nanocoating using $ZnSO_4$ as the precursor, whereas ZnO nanocoating was clearly observed using the combination of $ZnSO_4$ and $NaNO_3$ as the precursors.

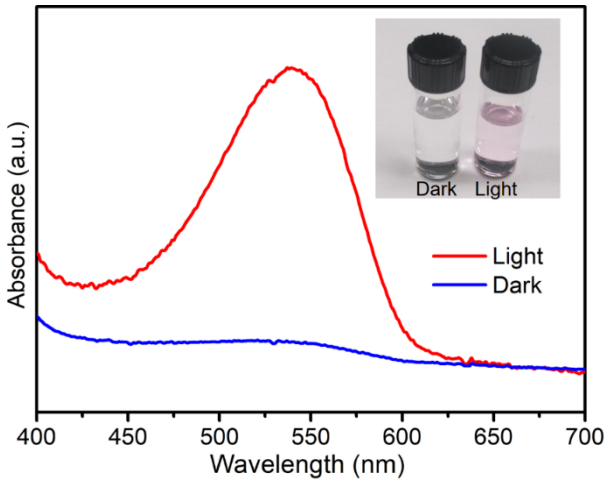

Fig. S24. UV-visible spectra of mixtures of Griess solution and photodeposition solution after the preparation of ZnO-deposited GaN sample (1 mL Griess reagent + 10 ml sample solution). A sample solution prepared under dark condition is shown for comparison. Inset is the optical image of the mixture solution. The absorbance peak at 540 nm indicates the presence of NO_2^- after the photodeposition process. The mechanism of the Griess reaction is a diazotization and coupling reaction as depicted below.[7,8] NO_2^- reacts with sulfanilamide (a) under acidic conditions to form the diazonium cation (b) which then couples to N-(1-naphthyl) ethylenediamine (c) for producing a red-violet colored azo dye (d), which strongly absorbs at 540 nm.

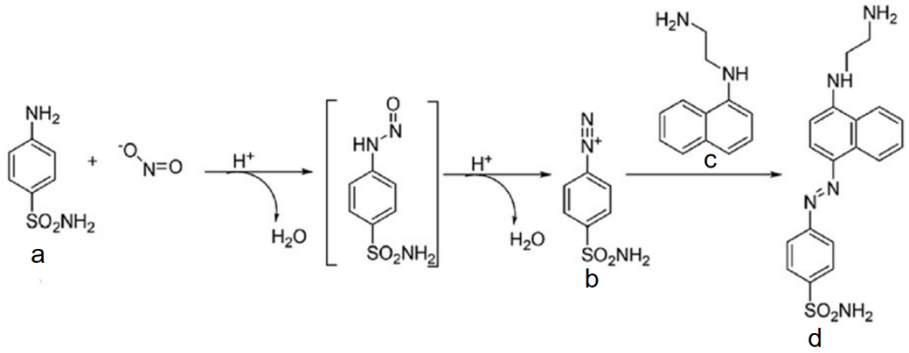

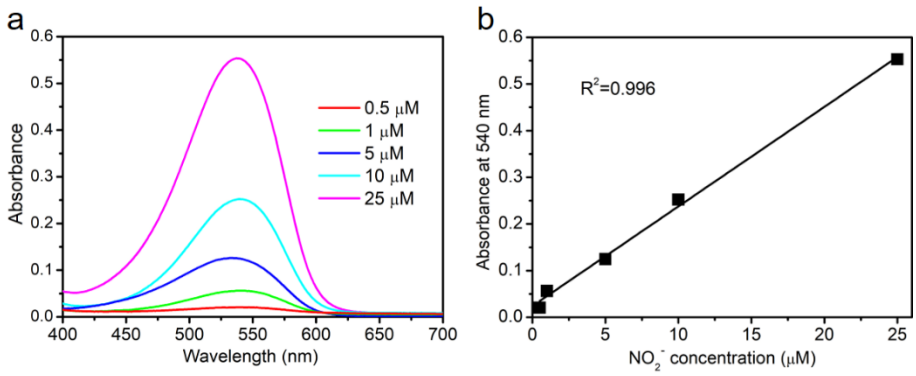

Fig. S25. (a) UV-visible spectra of mixtures of Griess solution and different concentrations of $NaNO_2$ (1 mL Griess reagent + 10 ml $NaNO_2$ solution). (b) The calibration curve of absorbance at wavelength of 540 nm versus $NaNO_2$ concentration. The absorbance at 540 nm of our NO_2^- solution after the photodeposition of ZnO was measured to be 0.09, indicating a NO_2^- concentration of 3.1 μM. Considering the solution volume of 75 mL, the produced NO_2^- amount was calculated to be 0.23 μmol.

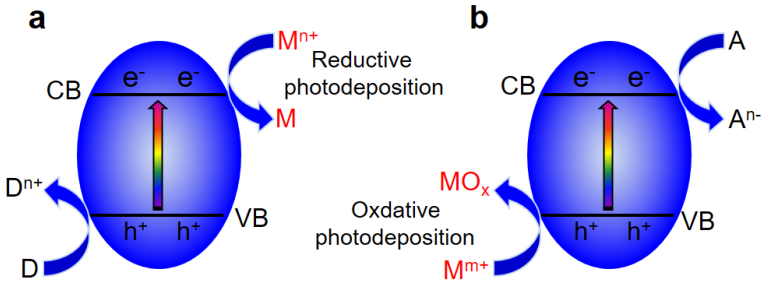

Fig. S26. Schematic of (a) reductive photodeposition and (b) oxidative photodeposition. CB: conduction band; VB: valence band; D: sacrificial electron donor; A: sacrificial electron acceptor.

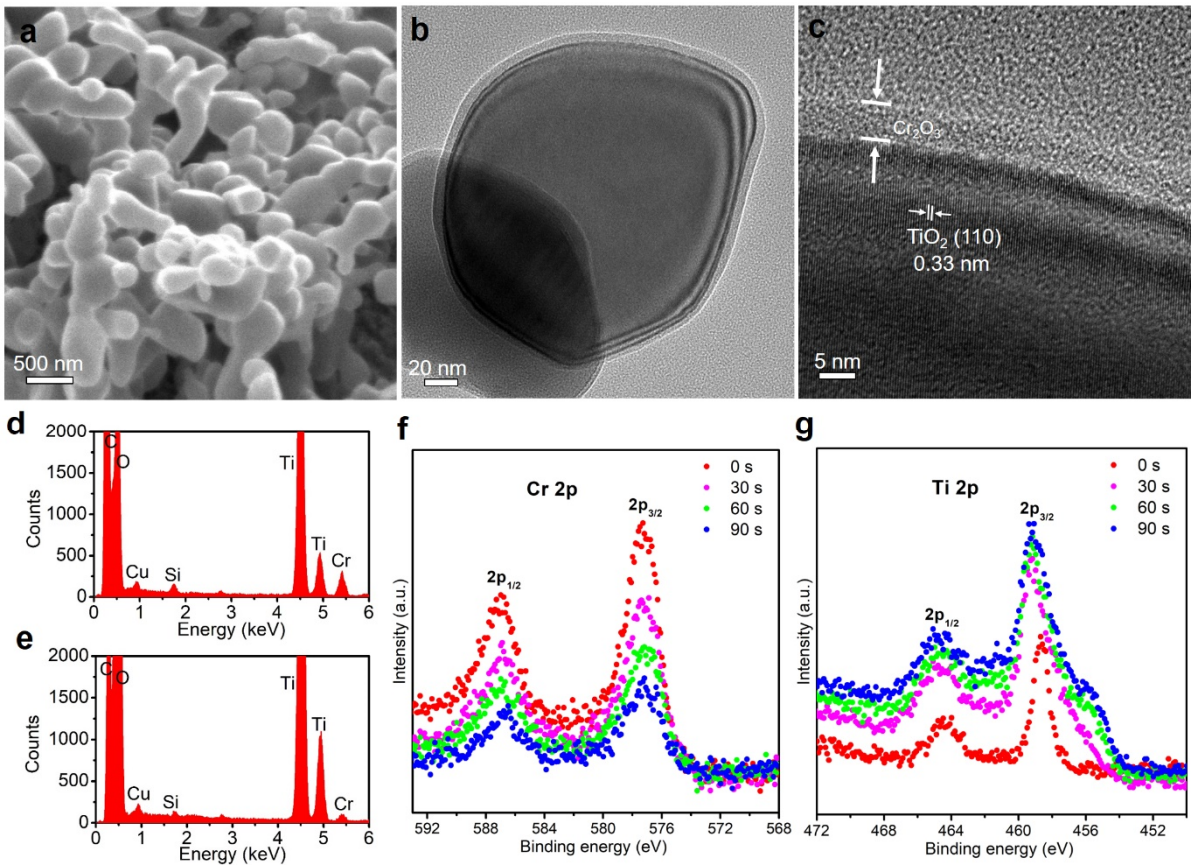

Fig. S27. (a) SEM, (b) TEM, (c) HRTEM images, and EDX analysis of the edge (d) and center region (e) of Cr_2O_3-deposited TiO_2 particle. XPS depth profiles of (f) Cr 2p and (g) Ti 2p in Cr_2O_3-deposited TiO_2 as a function of etching time. SEM shows the TiO_2 particle sizes are in the range between 200 and 500 nm. It indicates Cr_2O_3 coated on TiO_2 particle with high uniformity and conformality. The Cr_2O_3 layer is amorphous and has a thickness of ~5 nm. The EDX analysis of different particle regions and XPS depth profiles analysis confirm the TiO_2-Cr_2O_3 core-shell structure.

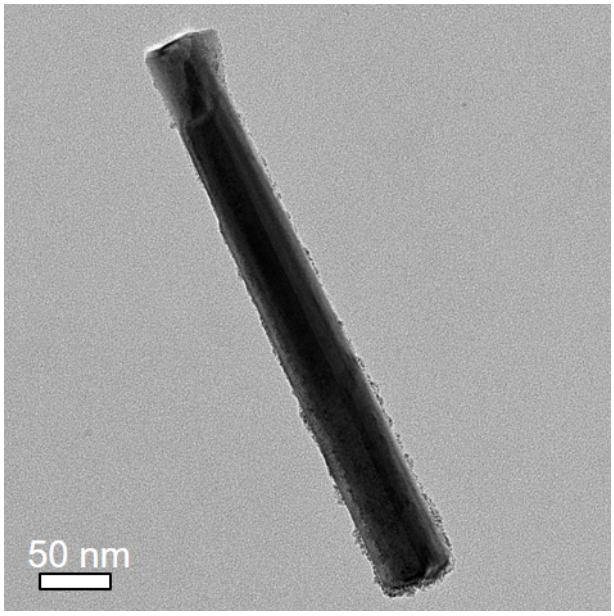

Fig. S28. TEM image of Cr_2O_3-coated GaN nanowire with Pt cocatalyst.

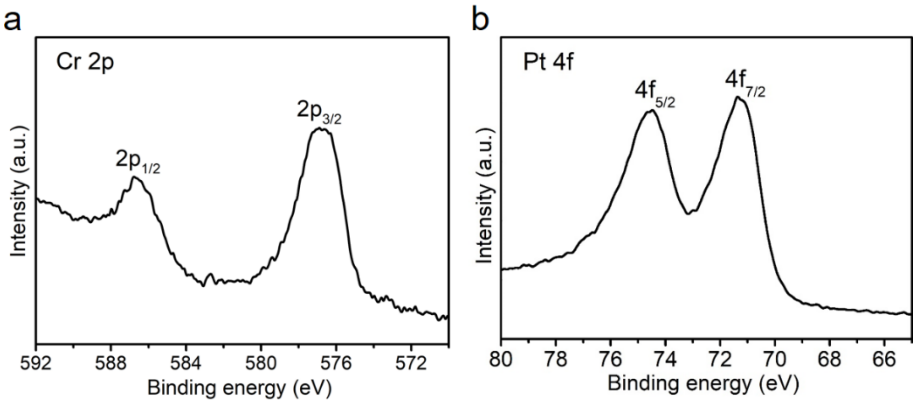

Fig. S29. XPS of (a) Cr 2p and (b) Pt 4f of $Pt/Cr_2O_3/GaN/n^+$–p Si sample. The Cr $2p_{3/2}$ binding energy at 576.9 eV and Cr $2p_{1/2}$ binding energy at 586.8 eV are assigned to Cr^{III} state from Cr_2O_3,[9] and Pt $4f_{7/2}$ binding energy at 71.3 eV and Pt $4f_{5/2}$ binding energy at 74.5 eV correspond to metallic Pt (Pt^0).[10]

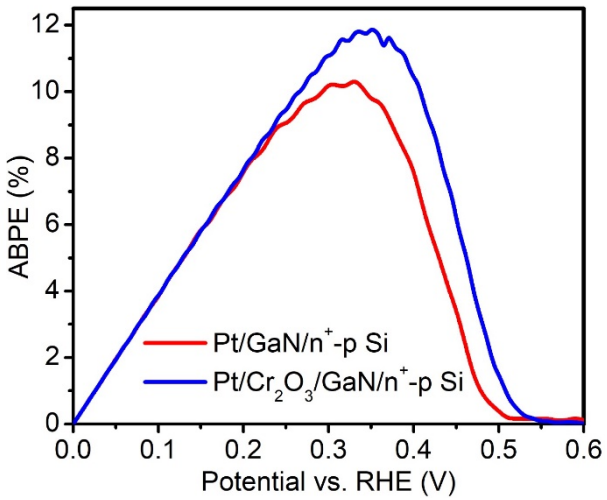

Fig. S30. ABPE of Pt/GaN/n^+–p Si and Pt/Cr_2O_3/GaN/n^+–p Si samples under AM 1.5G one-sun illumination. The maximum ABPE of Pt/Cr_2O_3/GaN/n^+–p Si is 11.8%, which is higher than that of Pt/GaN/n^+–p Si (10.4%).

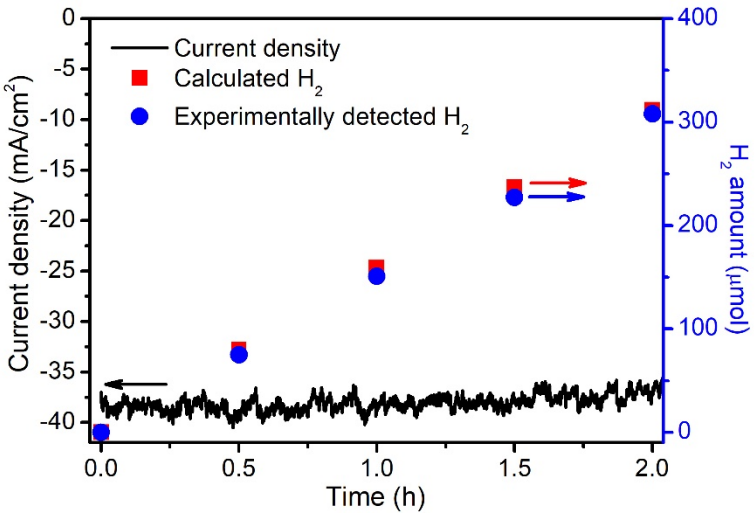

Fig. S31. Faradaic efficiency measurement of H_2 for Pt/Cr_2O_3/GaN/n^+–p Si photocathode at 0 V vs RHE. The calculated H_2 is the theoretical amount of H_2 produced assuming 100% Faraday efficiency.

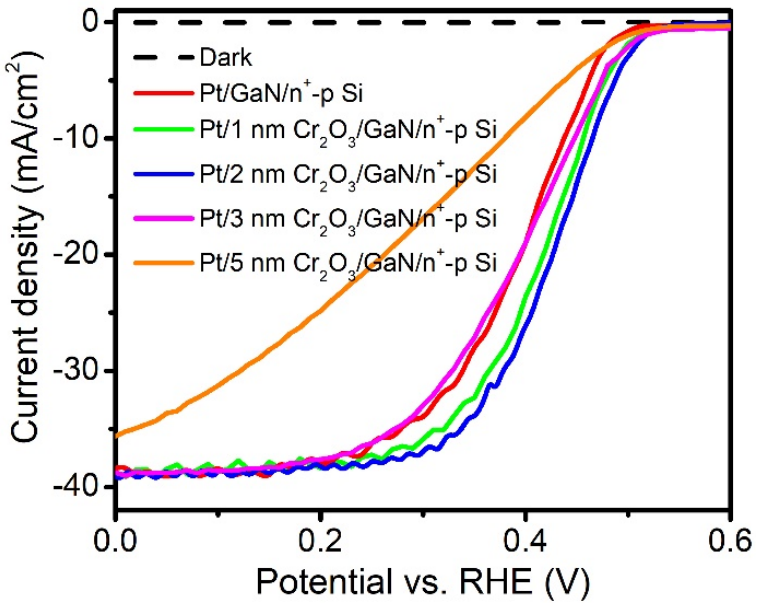

Fig. S32. *J-V* curves of Pt/Cr_2O_3/GaN/n^+–p Si samples with different Cr_2O_3 thicknesses under AM 1.5G one-sun illumination. The thickness of Cr_2O_3 was controlled by varying the $Cr(NO_3)_3$ precursor concentration. It was found that a thin Cr_2O_3 layer below 2 nm improve the PEC performance. Whereas increasing the Cr_2O_3 layer thickness beyond 2 nm resulted in diminished photocurrent, which can be ascribed to the large tunneling resistance to electron transport associated with a thick Cr_2O_3 layer.

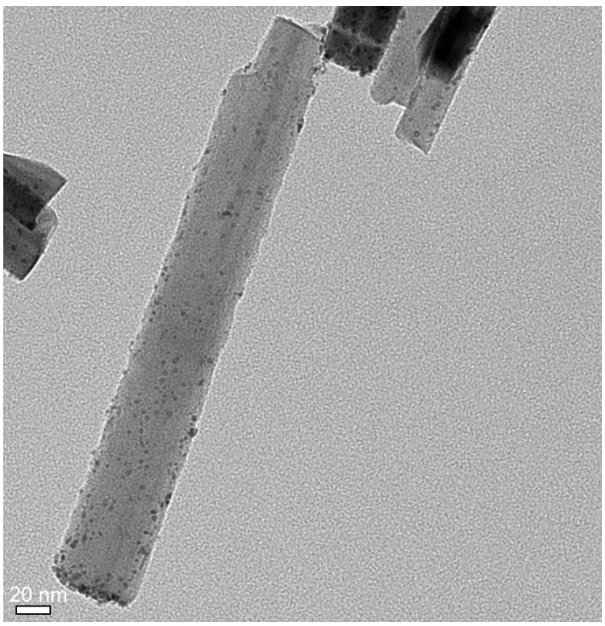

Fig. S33. TEM image of GaN nanowire with Pt cocatalyst. Compared to Pt/Cr_2O_3/GaN/n^+−p Si sample (Fig. S28, ESI†), the TEM image of Pt/GaN/n^+−p Si shows sparser distribution of Pt nanoparticles on nanowires. ICP-AES analysis indicates the loading amounts of Pt in Pt/GaN/n^+−p Si and Pt/Cr_2O_3/GaN/n^+−p Si samples were 4.6 and 6.8 nmol cm^{-2}, respectively.

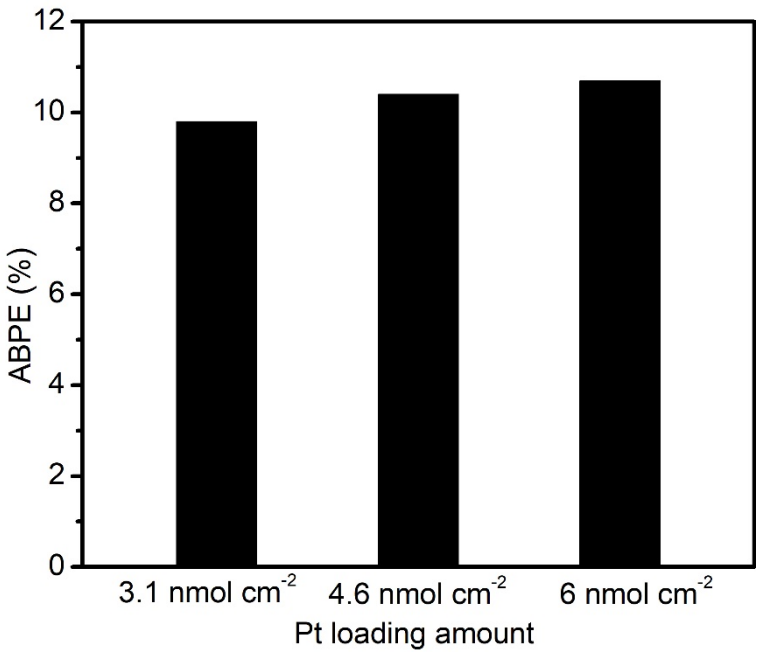

Fig. S34. Maximum ABPE of Pt/GaN/n^+–p Si samples as a function of Pt loading amount. By using 10, 15 and 20 μL of 0.2 M H_2PtCl_6 as precursors for the photodeposition, the loading amounts of Pt in Pt/GaN/n^+–p Si samples were determined by ICP-AES analysis to be 3.1, 4.6 and 6 nmol cm^{-2}, respectively. The loading amount of 6 nmol cm^{-2} Pt in Pt/GaN/n^+–p Si is comparable with that in Pt/Cr_2O_3/GaN/n^+–p Si (6.8 nmol cm^{-2}), whereas the maximum ABPE of Pt/GaN/n^+–p Si is 10.7%, which is lower than that of Pt/Cr_2O_3/GaN/n^+–p Si (11.8%). This indicates that the increase of Pt loading amount contributes partially to the enhanced PEC performance.

Table S1. Performance comparison between the presented $Pt/Cr_2O_3/GaN/n^+$-p Si photocathode and previously reported homojunction p-n Si-based photocathodes with ABPE >8% under AM 1.5G one-sun illumination.[a]

Photocathode	Onset potential (V vs RHE)	Current density at 0 V vs RHE (mA cm^{-2})	ABPE (%)	Ref
$Pt/Al_2O_3/n^+$-p Si	+0.52	30	8.7	11
$Pt/SiO_2/n^+$-p Si	+0.49	30	8.9	12
Pt/n^+-p Si	+0.56	28	9.6	13
Pt/n^+-p micropyramid Si	+0.53	36	10	14
Ni–Mo/NiSi/n^+-p microwire Si	+0.55	30	10.1	15
$Pt/GaN/n^+$-p Si	+0.5	38	10.5	16
$TiO_2/Pt/n^+$-p Si	+0.56	35	10.8	17
Ni–Mo/n^+-p microwire Si	+0.5	36	10.8	18
$IrO_x/TiO_2/F:SnO_2/Ti/n^+$-p Si	+0.56	39	10.9	19
$TiO_2/Pt/n^+np^+$ Si	+0.5	35	11.5	20
$Pt/Cr_2O_3/GaN/n^+$-p Si	+0.52	39	11.8	This work

[a] The highest ABPE reported for Si-based photocathodes is 13.26%,[21] which was achieved by a Si heterojunction structure consisting of amorphous Si (a-Si) layer on crystalline Si (c-Si) and thus not included in the Table. The record efficiency is largely attributed to the inherent high onset potential of +0.64 V vs RHE, which is much higher than that of common homojunction p-n Si-based photocathodes (≤ +0.56 V vs RHE).

Reference:

1 S. Chu, P. Ou, P. Ghamari, S. Vanka, B. Zhou, I. Shih, J. Song and Z. Mi, *J. Am. Chem. Soc.,* 2018, **140**, 7869-7877.

2 M. J. Moorcroft, J. Davis and R. G. Compton, *Talanta*, 2001, **54**, 785-803.

3 J. Peng, Q. J. Sun, Z. C. Zhai, J. Y. Yuan, X. D. Huang, Z. M. Jin, K. Y. Li, S. D. Wang, H. Q. Wang and W. L. Ma, *Nanotechnology*, 2013, **24**, 484010.

4 Y. T. Wang, J. Cheng, S. Y. Yu, E. J. Alcocer, M. Shahid, Z. Y. Wang and W. Pan, *Sci. Rep.,* 2016, **6**, 32711.

5 J. Y. Gan, X. H. Lu, J. H. Wu, S. L. Xie, T. Zhai, M. H. Yu, Z. S. Zhang, Y. C. Mao, S. C. I. Wang, Y. Shen and Y. X. Tong, *Sci. Rep.,* 2013, **3**, 1021.

6 L. Wang, S. Ouyang, B. Ren, J. Ye and D. Wang, *APL Mater.*, 2015, **3**, 104414.

7 D. Giustarini, R. Rossi, A. Milzani and I. Dalle-Donne, *Method Enzymol*, 2008, **440**, 361-380.

8 H. H. Wang, N. W. Wan, L. Ma, Z. Q. Wang, B. D. Cui, W. Y. Han and Y. Z. Chen, *Analyst*, 2018, **143**, 4555-4558.

9 K. Maeda, K. Teramura, D. L. Lu, N. Saito, Y. Inoue and K. Domen, *J. Phys. Chem. C*, 2007, **111**, 7554-7560.

10 Y. H. Li, J. Xing, Z. J. Chen, Z. Li, F. Tian, L. R. Zheng, H. F. Wang, P. Hu, H. J. Zhao and H. G. Yang, *Nat. Commun.*, 2013, **4**, 2500.

11 R. L. Fan, J. W. Min, Y. Li, X. D. Su, S. Zou, X. S. Wang and M. R. Shen, *Appl. Phys. Lett.*, 2015, **106**, 213901.

12 R. L. Fan, C. S. Tang, Y. Xin, X. D. Su, X. D. Wang and M. R. Shen, *Appl. Phys. Lett.*, 2016, **109**, 233901.

13 S. W. Boettcher, E. L. Warren, M. C. Putnam, E. A. Santori, D. Turner-Evans, M. D. Kelzenberg, M. G. Walter, J. R. McKone, B. S. Brunschwig, H. A. Atwater and N. S. Lewis, *J. Am. Chem. Soc.*, 2011, **133**, 1216-1219.

14 M. Caban-Acevedo, M. L. Stone, J. R. Schmidt, J. G. Thomas, Q. Ding, H. C. Chang, M. L. Tsai, J. H. He and S. Jin, *Nat. Mater.*, 2015, **14**, 1245-1251.

15 W. Vijselaar, R. M. Tiggelaar, H. Gardeniers and J. Huskens, *ACS Energy Lett.*, 2018, **3**,

1086-1092.

16 S. Vanka, E. Arca, S. Cheng, K. Sun, G. A. Botton, G. Teeter and Z. Mi, *Nano Lett.*, 2018, **18**, 6530-6537.

17 R. L. Fan, W. Dong, L. Fang, F. G. Zheng and M. R. Shen, *J. Mater. Chem. A*, 2017, **5**, 18744-18751.

18 W. Vijselaar, P. Westerik, J. Veerbeek, R. M. Tiggelaar, E. Berenschot, N. R. Tas, H. Gardeniers and J. Huskens, *Nat. Energy*, 2018, **3**, 185-192.

19 M. G. Kast, L. J. Enman, N. J. Gurnon, A. Nadarajah and S. W. Boettcher, *ACS Appl. Mater. Inter.*, 2014, **6**, 22830-22837.

20 Z. H. Yin, R. L. Fan, G. P. Huang and M. R. Shen, *Chem. Commun.*, 2018, **54**, 543-546.

21 H. P. Wang, K. Sun, S. Y. Noh, A. Kargar, M. L. Tsai, M. Y. Huang, D. L. Wang and J. H. He, *Nano Lett.*, 2015, **15**, 2817-2824.